optica

Dynamic hysteresis in a coherent high-β nanolaser

Si Hui Pan,[1] Qing Gu,[1,2] Abdelkrim El Amili,[1] Felipe Vallini,[1] and Yeshaiahu Fainman[1,*]

[1]Department of Electrical and Computer Engineering, University of California at San Diego, La Jolla, California 92093-0407, USA
[2]Department of Electrical Engineering, University of Texas at Dallas, Richardson, Texas 75080-3021, USA
*Corresponding author: fainman@ece.ucsd.edu

Received 25 July 2016; revised 20 September 2016; accepted 27 September 2016 (Doc. ID 272235); published 28 October 2016

The quest for an integrated light source that promises high energy efficiency and a fast modulation for high-performance photonic circuits has led to the development of room-temperature telecom-wavelength nanoscale lasers with a high spontaneous emission factor β. The coherence characterization of this type of laser using the conventional measurement of output light intensity versus input pump intensity is inherently difficult due to the diminishing kink in the measurement curve. We demonstrate that the transition from incoherent to coherent emission of a high-β pulse-pump metallo-dielectric nanolaser can be determined by examining the width of a second-order intensity correlation peak that shrinks below and broadens above the threshold. Our photon fluctuation study, the first ever reported for this type of nanolaser, confirms the validity of this measurement technique. Additionally, we show that the width variation above the threshold results from the delayed threshold phenomenon, providing the first observation of dynamical hysteresis in a nanolaser.

OCIS codes: (350.4238) Nanophotonics and photonic crystals; (190.1450) Bistability; (030.5290) Photon statistics; (030.1640) Coherence; (140.5960) Semiconductor lasers; (130.3120) Integrated optics devices.

http://dx.doi.org/10.1364/OPTICA.3.001260

1. INTRODUCTION

Nanocavity lasers with a high spontaneous emission factor β have attracted considerable attention in the past decade in light of their technical applications ranging from optical interconnects [1], biosensing [2], chemical detection [3], and nonlinear optical microscopy [4] to fundamental research on thresholdless lasers [5–8] and cavity quantum electrodynamics [9,10]. Theoretically, an extremely low lasing threshold is achievable with a high-beta nanolaser since most spontaneous emission is funneled into the lasing mode [5]. Additionally, the spontaneous emission rate can be significantly enhanced due to the Purcell effect in high-β nanoresonators, pushing the fundamental modulation speed limits of on-chip coherent sources to beyond 100 GHz [10]. A wide spectrum of resonator architectures has been explored, including photonic crystal cavities [7,8,11–14], circular [15] and rectangular [16] metallo-dielectric cavities, metal-semiconductor coaxial cavities [6], nanopillar/nanowire cavities [17,18], and plasmonic cavities (SPASERs) [19–23]. To date, the majority of studies on nanocavity lasers have focused on the proof of concept demonstration of lasing behavior. In particular, the measurement of a "kink" in the light-out versus light-in curve (LL-curve) is prevalently used as affirming evidence for lasing and is often the only method adopted to identify the lasing threshold [6,7,12,13,15–22]. However, it is well known that the "kink" in the LL-curve diminishes as β increases. Therefore, for high-β nanocavity lasers, LL-curve measurement alone can neither unequivocally confirm lasing nor unambiguously identify the lasing threshold.

On the other hand, measuring the second-order intensity correlation function $g^2(\tau) = \langle I(t)I(t+\tau)\rangle / \langle I(t)\rangle^2$, where $\langle I(t)\rangle$ represents the expectation value of the nanolaser output intensity at time t, is a more definitive method to confirm lasing [8,11,14,23]. The observation of a photon-bunching peak around zero delay ($\tau = 0$) signifies incoherent light emission and hence its suppression univocally marks the onset of coherent emission. In contrast to the LL-curve measurement, only a few $g^2(\tau)$ studies have been conducted with nanolasers due to their minuscule output power and relatively short coherence time. These constraints demand ultrasensitive photodetectors operating in the single-photon counting regime with excellent temporal precision. Commercial silicon-based single-photon detectors can meet these demands. Hence, most $g^2(\tau)$ studies so far have focused on nanoscale lasers emitting at wavelengths below 1 μm. Furthermore, these studies are conducted at cryogenic temperatures under continuous wave pumping, with either the family of photonic crystal cavity lasers [8,11] or plasmonic nanorod lasers [23]. With telecommunication wavelengths, however, $g^2(\tau)$ measurements become more challenging due to poorer detector time resolution, which is detrimental to the photon-bunching peak. Optical pulse pumping typically employed for nanolasers further complicates the measurement because the photon-bunching peak overlaps with only the zero-delay pulse. Therefore, the difference in height between the zero-delay and non-zero-delay pulses is the only indication that the bunching peak exists, while its specific shape usually cannot be observed. Further, optical misalignment,

signal-to-noise ratio, and other measurement artifacts such as detector crosstalk [24] can also affect the height difference, compromising its accuracy.

In this study, we show that by employing nanosecond pump pulses, different emission regimes of a nanolaser can be characterized via the full width at half-maximum (FWHM) of a $g^2(\tau)$ peak. We demonstrate the applicability of this technique with a high-β metallo-dielectric nanolaser and further report the first coherence measurement on this type of nanolaser operating at room temperature. We show that while $g^2(\tau)$ peaks narrow in the spontaneous emission (SE) and amplified spontaneous emission (ASE) regimes as stimulated emission increases in proportion, their FWHMs increase in the lasing regime due to dynamical hysteresis (DH), a phenomenon triggered when a laser is driven across its threshold. The usage of nanosecond pulses is the key to the observation of DH and, therefore, essential to this characterization technique. Previous $g^2(\tau)$ studies utilizing picosecond [14] or femtosecond [25] pulses could not observe this phenomenon because the resulting output pulse widths are far below the photodetector's time resolution, which is typically on the order of a hundred picoseconds.

2. RESULTS AND DISCUSSION

A. Device Architecture and Photoluminescence Spectra

The metallo-dielectric nanocavity design, shown in Fig. 1(a), and fabrication techniques used in this study follow those of Nezhad *et al.* [15, see Supplement 1, Sections 1 and 2 for details]. Detailed experimental techniques are presented in Supplement 1, Section 3. Scanning electron microscope (SEM) images of the device after dry etching and silver sputtering are shown in Figs. 1(b) and 1(c), respectively. The measured spectral evolution of the device from below to above the threshold is presented in Fig. 1(d). Broadband photoluminescence (PL) spectra at low pump intensities indicate that the emission is predominantly spontaneous. As the pump intensity increases, a narrow spectral line appears at around 1421 nm, corresponding to the lasing mode. The emission linewidth narrows with increasing pump intensity below threshold, showing good agreement with the Schawlow–Townes theory (see Supplement 1, Section 4). The integrated output power from the PL spectra as a function of the input pump intensity in a log-log scale (LL-curve) is presented in Fig. 2(a). Using a rate-equation model (see Supplement 1, Section 5) with a time-dependent pump pulse and β as a free parameter, we were able to fit the experimental LL-curve and obtain a β factor of 0.25. The different operational regimes of our nanolaser, including SE, ASE, and stimulated emission, are clearly identified in the LL-curve. The threshold intensity I_{th} as conventionally defined by the kink in the LL-curve, is approximately 2.5 kW/mm^2.

B. Photon Statistics

To further verify that the nano device is indeed a laser, we first examined the normalized intensity correlation at zero delay $g^2(0)$ as a function of pump intensity [Fig. 2(b)]. The points labeled as I, II, and III in Fig. 2(b) were calculated from the experimental nonnormalized correlation histograms shown in Figs. 3(a)–3(f), respectively. Regardless of the output photon statistics of our device, the nonnormalized correlation histograms are expected to

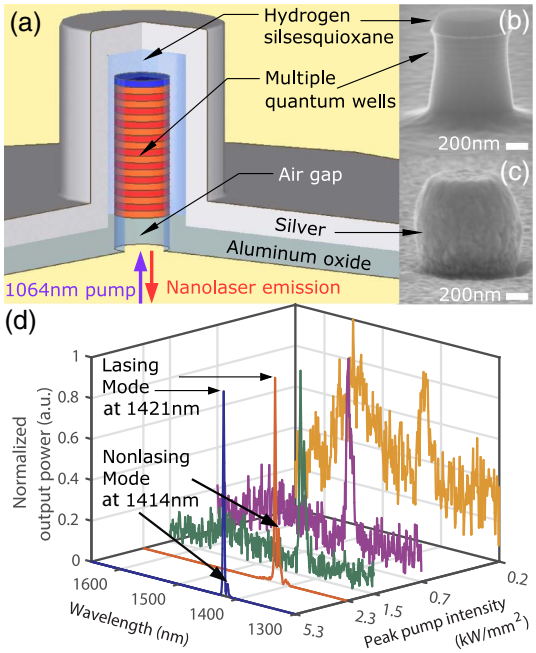

Fig. 1. (a) A schematic of the fabricated metallo-dielectric nanolaser: 300 nm of multiple quantum wells gain medium is surrounded by 100 nm of oxide, which is covered by 300 nm of silver. (b) and (c) SEM images of the nanolaser after (b) reactive ion etching and (c) silver deposition. (d) Normalized spectral evolution of our high-β nanolaser indicates a broadband spontaneous emission spectrum at low pump intensities and a distinct lasing peak (1421 nm) accompanied by a nonlasing mode (1414 nm) at high pump intensities.

have pulses at a frequency equivalent to the pump laser repetition rate, as depicted in Figs. 3(a)–3(c). In addition, the output emission of the device exhibits super-Poissonian light characteristics [$g^2(\tau = 0) > 1$] before lasing occurs. Hence, in the SE and ASE regimes, extra correlation counts due to photon bunching will be added to the zero-delay pulse, making it taller than the nonzero-delay pulses [Figs. 3(b) and 3(e)]. As the nanolaser transitions from below to above the threshold, the emitted photons statistics evolves from super-Poissonian to Poissonian. Therefore, the extra bunching peak disappears and the zero-delay pulse height approaches that of a nonzero-delay pulse [Figs. 3(c) and 3(f)], indicating coherent light emission [$g^2(\tau = 0) = 1$]. Careful examination of Fig. 2(b) shows that $g^2(0)$ reaches unity within the measurement error when the pump intensity is equal to or greater than 7.5 kW/mm^2 or three times I_{th}. Therefore, although stimulated emission begins to dominate at the kink of the LL-curve, signifying the onset of lasing, a high degree of coherence is not achieved in the light emission until at pump intensities far beyond not only the kink but also the ASE region defined by the nonlinear increase in the LL-curve. Similar results have been reported for lasers based on micropillar cavities [26] and photonic crystal cavities [8,14]. The slight difference between $g^2(0)$ and unity at $I_{\text{peak}} > 7.5$ kW/mm^2, as observed in Fig. 2(b), is most likely due to a small amount of incoherent light emitted into a nonlasing mode at 1414 nm [see Fig. 1(d)]. Meanwhile, Figs. 3(a) and 3(d) shows that the photon-bunching peak also disappears far below the threshold instead of approaching the theoretical value of two [$g^2(\tau = 0) = 2$] expected for an ideal thermal light source. This is because the coherence time τ_c is

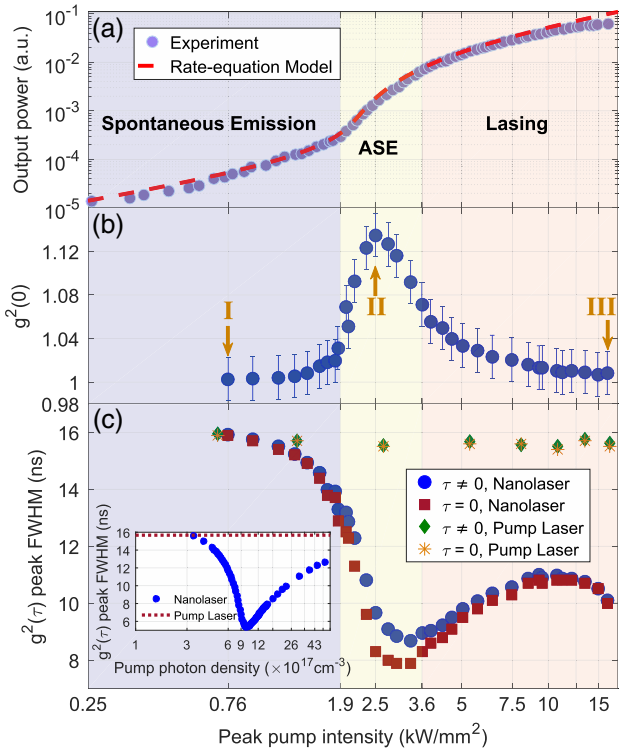

Fig. 2. (a) LL-curve: experimental (circles) and theoretical (dashed line) output power of the nanolaser as functions of input pump intensity. The theoretical LL-curve is generated by fitting the experimental data with a rate-equation model. The SE factor β is fitted to be 0.25. (b) The evolution of the nanolaser's second-order intensity correlation function at zero delay $g^2(0)$, which confirms lasing as it approaches unity at high pump intensities. It decays at low pump intensities because the coherence time drops below the detection limit of our setup. (c) The experimental FWHM of the nanolaser and pump laser $g^2(\tau)$ pulses as functions of the pump intensity. The FWHM narrows below the threshold due to the increasing radiative recombination rate as stimulated emission increases in fraction. Above the threshold, the DTP or DH leads to broadening of the FWHM until self-heating dominates beyond 12.5 kW/mm^2 of pump intensity, at which point width narrowing is again observed. The inset plots the theoretical FWHM simulated with a rate-equation model without considering self-heating.

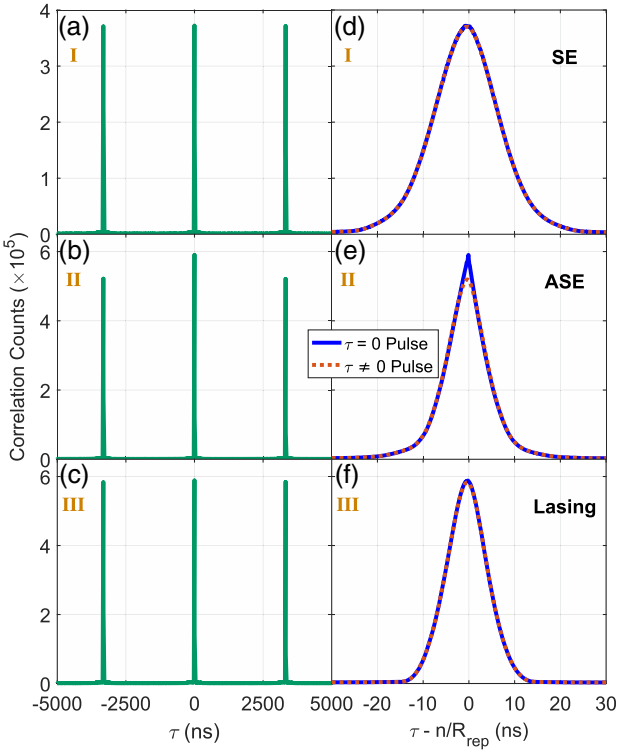

Fig. 3. (a)–(c) Measured histograms at pump intensities labeled as I, II, and III in Fig. 2(b), corresponding to the SE, ASE, and lasing regimes of the nanolaser. (d)–(f) are the same as (a)–(c) but with the nonzero-delay pulses overlaid on top of the zero-delay pulses. In the SE regimes (a) and (d), the coherence time of the source is too short to be resolved by the photodetectors, resulting in the disappearance of the photon-bunching peak. In the ASE regimes (b) and (e), the coherence time lengthens and the photon-bunching peak emerges, indicating that the emission is partially incoherent. The photon-bunching peak disappears in (c) and (f) eventually when the nanolaser emission becomes fully coherent at high pump intensities. Additionally, the pulse FWHM varies at different emission regimes, with the broadest width appearing in the SE regime.

extremely short compared to the time resolution of the photodetectors (~100 ps) when SE dominates. The width of the photon-bunching peak is on the order of the coherence time [27]. Thus, as τ_c decreases, the averaging effect due to the detector timing uncertainty gradually washes out the "fingerprint" of the super-Poissonian statistics below the threshold.

C. Intensity Correlation Peak FWHM Analysis

1. Experimental Results

While the pulse height difference has been previously observed and used to demonstrate lasing [14,25], we show here the very first detailed investigation of the pulse width variation at different emission regimes of a nanolaser. Comparisons between Figs. 3(d)–3(f) indicate that the $g^2(\tau)$ pulses are the widest in the SE regime while the width variations in the ASE and the lasing regimes are subtler. We extract the $g^2(\tau)$ pulse FWHM from the experimental correlation histogram and plot it as a function of the pump intensity from far below to far above the threshold in Fig. 2(c). As shown, the pulses narrow as the pump intensity increases in the SE regime and reach a minimum in the ASE regime. The pulses then broaden as the pump intensity further increases in the lasing regime until it reaches more than four times the intensity of I_{th} when pulse narrowing is observed again. The zero-delay pulse is narrower than the nonzero-delay pulses around the threshold due to an extra photon-bunching peak, as discussed above. Given the large delay-time intervals between adjacent pulses ($\Delta\tau \sim 3$ μs) in $g^2(\tau)$, the change in the photon statistics described above affects only the zero-delay pulse, and therefore cannot account for the pulse narrowing or broadening behaviors that apply to both the nonzero-delay and zero-delay pulses. Meanwhile, the distinct evolutional trends in the FWHM before and after lasing occurs indicate their close relationship to the nanolaser operational regimes. To ensure that the observed FWHM variation is not caused by modifications in the pump laser itself, we also characterize the FWHM of the pump laser $g^2(\tau)$ as a function of the pump intensity [Fig. 2(c)]. The results, which are taken over several hours and repeatable on a daily basis, reveal negligible variations in the pump laser $g^2(\tau)$ width, confirming that the pulse narrowing and broadening effects results primarily from the nanolaser operation mechanism.

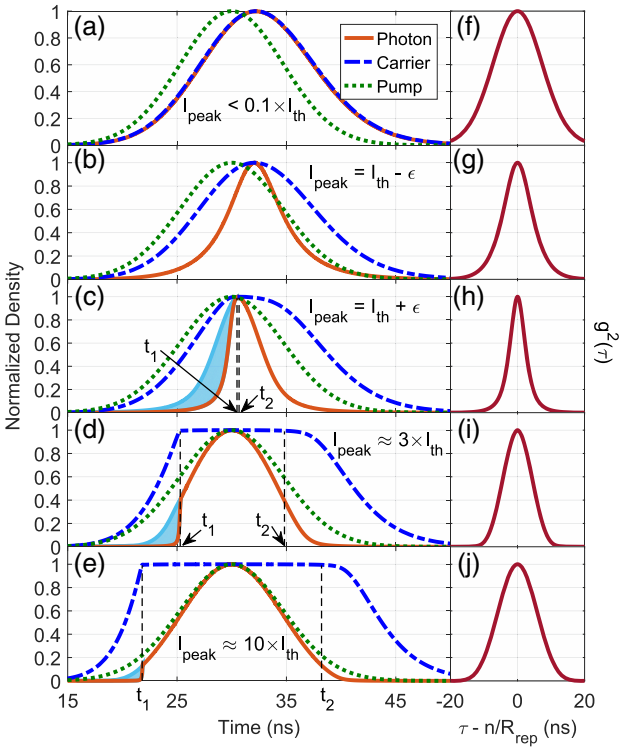

Fig. 4. (a)–(e), Normalized output photon, carrier, and pump (injection) photon densities as functions of time at peak pump intensities I_{peak}, (a) far below threshold, (b) slightly below threshold, (c) slightly above threshold, and (d) and (e) far above threshold. The black dashed lines and labels t_1 and t_2 in (c), (d), and (e) indicate when the pump pulse crosses I_{th}. The output photon pulse follows the shape of the pump pulse in (a) the SE regime, but narrows as (b) the pump intensity increases. In the far below threshold regime, the narrowing rate is predominantly influenced by the SE lifetime. (c)–(e) Above the threshold, the DTP-induced DH is observed, truncating part of the photon pulse (see the blue shaded regions), which leads to an asymmetrical pulse shape. As the pump intensity increases above the threshold, the pump pulse crosses the threshold at a smaller t_1 and the DH effect trims away less of the output (i.e., blue shaded regions reduce in area), leading to pulse broadening. (f)–(j) The normalized autocorrelations $g^2(\tau)$, of the photon pulses shown in (a)–(e). The cross correlations of neighboring photon pulses are identical to the autocorrelations, but are located at $\tau_n = n/R_{rep}$. By definition, $g^2(\tau)$ pulses are symmetrical, but their FWHM is proportional to those of the output photon pulses and, therefore, retain the width information of the output photon pulse. The FWHM of the pulses shown are (f) 17.32, (g) 9.86, (h) 5.38, (i) 9.94, and (j) 13.38 [ns].

2. Rate-Equation Simulation Reveals Dynamical Hysteresis

To further understand the mechanism governing the pulse width evolution, we employ a rate-equation model to examine the output photon and carrier densities as functions of time (see Supplement 1, Section 5). Figure 4 shows the theoretical responses of the nanolaser subjected to a time-dependent Gaussian pump pulse at peak intensities far below the threshold [Fig. 4(a)], slightly below the threshold [Fig. 4(b)], slightly above the threshold [Fig. 4(c)], and far above the threshold [Figs. 4(d) and 4(e)]. By taking the autocorrelation (see Supplement 1, Section 5) of the photon pulses shown in Figs. 4(a)–4(e), the $g^2(\tau)$ functions are generated numerically and shown in Figs. 4(f)–4(j). The FWHM of the simulated $g^2(\tau)$ pulse as a function of the pump intensity is plotted in the inset of Fig. 2(c). In the SE regime, the width of the output optical pulse is primarily determined by the pump pulse width [Fig. 4(a)], the photon lifetime (τ_p), and the radiative recombination lifetime (τ_{rc}), which can be approximated by the SE lifetime in this far below threshold region. As the peak pump intensity increases, the stimulated emission grows in contribution and the device gradually transitions to the ASE regime. Stimulated emission accelerates radiative recombination in the cavity, which reduces the width of the output optical pulse [Fig. 4(b)]. This pulse-shortening phenomenon contributes to the narrowing effect in the SE and ASE regions of Fig. 2(c). Additionally, the narrowing rate here is significantly influenced by τ_{rc}, which is reduced due to the prominent Purcell effect in nanocavity lasers [9,10]. We found a satisfactory agreement between theory and experiment when $\tau_{rc} = 2$ ns [Fig. 2(c) and inset]. Comparison between this value and the radiative recombination lifetime of a multiple quantum wells wafer, where $\tau_{rc} \approx 100$ ns [28], gives a Purcell enhancement factor of approximately 50, which is consistent to the same order of magnitude with the value 53 estimated by the method used in Refs. [9,15].

As the peak pump intensity continues to increase, the FWHM reaches a minimum at around the threshold and begins to broaden. Such a broadening effect is a consequence of the delayed threshold phenomenon (DTP), which arises when any nonlinear system crosses a bifurcation point between two stable solution branches [29,30]. In a laser, the bifurcation point corresponds to the lasing threshold and the DTP manifests itself in the form of a jump in the output intensity when the pump intensity is swept across the threshold. Such a phenomenon has been previously observed in macroscopic lasers [31–33]. Figures 4(c)–4(e) show that the DTP is also present in our nanolaser. As the time-dependent Gaussian pump pulse sweeps across the nanolaser threshold I_{th} at time t_1 [Figs. 4(c)–4(e)], the nonlinear system does not respond immediately due to the infinite response time at the bifurcation point I_{th} [30]. Physically stimulated emission cannot happen instantaneously. The time it takes to generate enough stimulated photons to statistically dominate the emission depends on the nanolaser characteristic times, such as the photon and carrier lifetimes. Hence, the nanolaser remains in its nonlasing state for some time after the pump pulse intensity crosses I_{th}. When stimulated emission finally builds up in the cavity such that the nanolaser switches to its lasing state, the output photon intensity increases by more than an order of magnitude in a very short time period (~1 ns). This fast change in intensity truncates part of the output pulse on the left-hand side, leading to an asymmetrical pulse shape. The missing parts of the photon pulses are represented by blue shaded regions in Figs. 4(c)–4(e). The nanolaser remains in the lasing state for as long as $I(t) < I_{th}$. However, once the pump intensity reduces to below I_{th} at time t_2, lasing ceases and the device gradually decays back to its initial state. Unlike the transition from nonlasing to lasing, the reverse process happens smoothly because the cavity is already filled with photons whose number gradually decays to zero after t_2. The decaying process happens continuously. Therefore, no sudden change in intensity is observed on the right-hand side of the output pulse. This asymmetry between the response of the laser when the pump is swept from below to above the threshold and vice versa is often termed as dynamical hysteresis in the literature [29,30,33].

Above the threshold, a higher peak pump intensity corresponds to a smaller t_1 [Figs. 4(c)–4(e)]. Therefore, the intensity

jump on the left-hand side of the output pulse happens at an earlier time, which trims away less of the photon pulse, as indicated by the reducing areas of the blue shaded regions with increasing peak pump intensities in Figs. 4(c)–4(e). This is consistent with the fact that the time delay associated with the DTP reduces as the first derivative of the pump pulse increases proportionally to the peak pump intensity (see Figs. S3–S5 in Supplement 1, Section 5) [29–33]. Additionally, as the pump pulse stays above the threshold for a longer period of time, the device continues lasing for longer and the photon decay on the right-hand side of the output pulse happens at a later time. That is $\Delta t = t_2 - t_1$ increases since t_1 decreases while t_2 increases. All these factors contribute to a longer output pulse, which leads to broadening of the $g^2(\tau)$ functions as the peak pump intensity increases above the threshold [Fig. 2(c)]. Theoretically, at a very high peak intensity, $\Delta t = t_2 - t_1$ approaches infinity and nearly the entire pump pulse is above the threshold. At this point, the output pulse mirrors the pump and its width is determined entirely by the width of the pump pulse. However, in order to reach this condition, the peak intensity must be at least a hundred times above the threshold (see Fig. S6 in Supplement 1, Section 5), which is unachievable in practical experiments.

In fact, as shown in Fig. 2(c), the experimental curve deviates far from theory once the peak pump intensity becomes more than 7.5 kW/mm^2 or three times the threshold intensity. Such a discrepancy can be explained by thermal saturation of the device at high pump intensities, which is unaccounted for in our rate-equation model. Above the threshold, gain material properties degrade as a result of a rapid internal temperature rise in the device with increasing pump intensities, which reduces the device internal quantum efficiency. In addition, metal losses are proportional to temperature. Therefore, the quality factor is expected to reduce as a result of self-heating. In combination, these effects cause an increase in the nanolaser threshold [34,35], which is effectively equivalent to reducing the pump (or injected) carrier density. Therefore, self-heating of the device leads to a reduction in the $g^2(\tau)$ pulse width far above threshold. Consequently, the above-threshold behavior of the $g^2(\tau)$ FWHM depends on the interplay between broadening due to DH and narrowing due to self-heating. Below three times the threshold, $I_{\text{peak}} < 3I_{\text{th}} = 7.5$ kW/mm^2, width broadening due to DH dominates and the experimental data follow the same trend predicted by theory [Fig. 2(c) inset]. Above three times the threshold, corresponding to when the nanolaser emission is fully coherent, the narrowing effect due to self-heating balances the DTP-induced broadening and the experimental FWHM stays approximately constant. Beyond five times the threshold intensity, self-heating dominates and pulse width narrowing is again observed for the last three pump intensities. Thermal saturation also causes roll-over in the LL-curve at high pump intensities [33], which predicts the measured laser output intensities to be less than the theoretical values given by our rate-equation model. Such a difference has been observed in our experimental data [Fig. 2(a)], confirming the existence of self-heating at high pump intensities.

3. SUMMARY

In summary, we examined the $g^2(\tau)$ pulse width as a function of the pump intensity and demonstrated that the width evolution is closely linked to the different operational regimes of our high-β metallo-dielectric nanolaser whose lasing behavior has been confirmed by both LL-curve and second-order intensity correlation at zero delay. We demonstrated that the $g^2(\tau)$ pulses shrink in width below and near the threshold and broaden above the threshold when nanosecond pump pulses are employed. It is, therefore, feasible to exploit such a measurement technique to identify the SE, ASE, and lasing regimes of a near-unity-β nanolaser, such as those reported by Khajavikhan *et al.* [6] and Oulton *et al.* [21], when its LL-curve fails to be reliable due to its diminishing kink. By exploring a rate-equation model, we discover that the modified SE lifetime of our nanocavity heavily influences the below threshold narrowing rate of the $g^2(\tau)$ pulses, offering valuable information about the Purcell factor that neither the LL-curve nor the $g^2(0)$ measurement could provide. On the other hand, dynamical hysteresis and the self-heating effect determine the above threshold behavior of the $g^2(\tau)$ pulse width. While dynamical hysteresis in macroscopic lasers has been studied before, this is the first time such nonlinear dynamics have been observed in a nanolaser through the second-order intensity correlation measurement. Our work demonstrates that a second-order intensity correlation measurement conducted under pulse pumping in the nanosecond time scale can be utilized to extract information about the nonlinear dynamics and Purcell factor of nanolasers in addition to confirming the Poisson statistics of their output. This work paves the way for future investigations of the photon statistics of unity-β nanolasers as well as the unexplored physics of nonlinear dynamics in ultra-small resonators.

Funding. National Science Foundation (NSF); Office of Naval Research (ONR); Army Research Office (ARO); Cymer; National Science Foundation Graduate Research Fellowship (NSFGRF) (DGE-1144086).

Acknowledgment. S. H. P. is a recipient of the NSFGRF and would like to thank the NSFGRF for partial support for her graduate study.

See Supplement 1 for supporting content.

REFERENCES

1. D. A. B. Miller, "Are optical transistors the logical next step?" Nat. Photonics **4**, 3–5 (2010).
2. G. Shambat, S.-R. Kothapalli, J. Provine, T. Sarmiento, J. Harris, S. S. Gambhir, and J. Vučković, "Single-cell photonic nanocavity probes," Nano Lett. **13**, 4999–5005 (2013).
3. M. Lončar, A. Scherer, and Y. Qiu, "Photonic crystal laser sources for chemical detection," Appl. Phys. Lett. **82**, 4648–4650 (2003).
4. Y. Nakayama, P. J. Pauzauskie, A. Radenovic, R. M. Onorato, R. J. Saykally, J. Liphardt, and P. Yang, "Tunable nanowire nonlinear optical probe," Nature **447**, 1098–1101 (2007).
5. S. Noda, "Seeking the ultimate nanolaser," Science **314**, 260–261 (2006).
6. M. Khajavikhan, A. Simic, M. Katz, J. H. Lee, B. Slutsky, A. Mizrahi, V. Lomakin, and Y. Fainman, "Thresholdless nanoscale coaxial lasers," Nature **482**, 204–207 (2012).
7. I. Prieto, J. M. Llorens, L. E. Muñoz-Camúñez, A. G. Taboada, J. Canet-Ferrer, J. M. Ripalda, C. Robles, G. Muñoz-Matutano, J. P. Martínez-Pastor, and P. A. Postigo, "Near thresholdless laser operation at room temperature," Optica **2**, 66–69 (2015).
8. Y.-S. Choi, M. T. Rakher, K. Hennessy, S. Strauf, A. Badolato, P. M. Petroff, D. Bouwmeester, and E. L. Hu, "Evolution of the onset of coherence in a family of photonic crystal nanolasers," Appl. Phys. Lett. **91**, 031108 (2007).

9. J. M. Gerard and B. Gayral, "Strong Purcell effect for InAs quantum boxes in three-dimensional solid-state microcavities," J. Lightwave Technol. **17**, 2089–2095 (1999).
10. H. Altug, D. Englund, and J. Vučković, "Ultrafast photonic crystal nanocavity laser," Nat. Phys. **2**, 484–488 (2006).
11. S. Strauf, K. Hennessy, M. T. Rakher, Y.-S. Choi, A. Badolato, L. C. Andreani, E. L. Hu, P. M. Petroff, and D. Bouwmeester, "Self-tuned quantum dot gain in photonic crystal lasers," Phys. Rev. Lett. **96**, 127404 (2006).
12. H.-G. Park, S.-H. Kim, S.-H. Kwon, Y.-G. Ju, J.-K. Yang, J.-H. Baek, S.-B. Kim, and Y.-H. Lee, "Electrically driven single-cell photonic crystal laser," Science **305**, 1444–1447 (2004).
13. B. Ellis, M. A. Mayer, G. Shambat, T. Sarmiento, J. Harris, E. E. Haller, and J. Vučković, "Ultralow-threshold electrically pumped quantum-dot photonic-crystal nanocavity laser," Nat. Photonics **5**, 297–300 (2011).
14. R. Hostein, R. Braive, L. Le Gratiet, A. Talneau, G. Beaudoin, I. Robert-Philip, I. Sagnes, and A. Beveratos, "Demonstration of coherent emission from high-β photonic crystal nanolasers at room temperature," Opt. Lett. **35**, 1154–1156 (2010).
15. M. P. Nezhad, A. Simic, O. Bondarenko, B. Slutsky, A. Mizrahi, L. Feng, V. Lomakin, and Y. Fainman, "Room-temperature subwavelength metallo-dielectric lasers," Nat. Photonics **4**, 395–399 (2010).
16. M. T. Hill, Y.-S. Oei, B. Smalbrugge, Y. Zhu, T. de Vries, P. J. van Veldhoven, F. W. M. van Otten, T. J. Eijkemans, J. P. Turkiewicz, H. de Waardt, E. J. Geluk, S.-H. Kwon, Y.-H. Lee, R. Nötzel, and M. K. Smit, "Lasing in metallic-coated nanocavities," Nat. Photonics **1**, 589–594 (2007).
17. R. Chen, T.-T. D. Tran, K. W. Ng, W. S. Ko, L. C. Chuang, F. G. Sedgwick, and C. Chang-Hasnain, "Nanolasers grown on silicon," Nat. Photonics **5**, 170–175 (2011).
18. D. Saxena, S. Mokkapati, P. Parkinson, N. Jiang, Q. Gao, H. H. Tan, and C. Jagadish, "Optically pumped room-temperature GaAs nanowire lasers," Nat. Photonics **7**, 963–968 (2013).
19. D. J. Bergman and M. I. Stockman, "Surface plasmon amplification by stimulated emission of radiation: quantum generation of coherent surface plasmons in nanosystems," Phys. Rev. Lett. **90**, 027402 (2003).
20. M. A. Noginov, G. Zhu, A. M. Belgrave, R. Bakker, V. M. Shalaev, E. E. Narimanov, S. Stout, E. Herz, T. Suteewong, and U. Wiesner, "Demonstration of a spaser-based nanolaser," Nature **460**, 1110–1112 (2009).
21. R. F. Oulton, V. J. Sorger, T. Zentgraf, R.-M. Ma, C. Gladden, L. Dai, G. Bartal, and X. Zhang, "Plasmon lasers at deep subwavelength scale," Nature **461**, 629–632 (2009).
22. R.-M. Ma, R. F. Oulton, V. J. Sorger, and X. Zhang, "Plasmon lasers: coherent light source at molecular scales," Laser Photon. Rev. **7**, 1–21 (2013).
23. Y.-J. Lu, J. Kim, H.-Y. Chen, C. Wu, N. Dabidian, C. E. Sanders, C.-Y. Wang, M.-Y. Lu, B.-H. Li, X. Qiu, W.-H. Chang, L.-J. Chen, G. Shvets, C.-K. Shih, and S. Gwo, "Plasmonic nanolaser using epitaxially grown silver film," Science **337**, 450–453 (2012).
24. I. Rech, A. Ingargiola, R. Spinelli, I. Labanca, S. Marangoni, M. Ghioni, and S. Cova, "Optical crosstalk in single photon avalanche diode arrays: a new complete model," Opt. Express **16**, 8381–8394 (2008).
25. S. Kim, B. Zhang, Z. Wang, J. Fischer, S. Brodbeck, M. Kamp, C. Schneider, S. Höfling, and H. Deng, "Coherent polariton laser," Phys. Rev. X **6**, 011026 (2016).
26. S. M. Ulrich, C. Gies, S. Ates, J. Wiersig, S. Reitzenstein, C. Hofmann, A. Löffler, A. Forchel, F. Jahnke, and P. Michler, "Photon statistics of semiconductor microcavity lasers," Phys. Rev. Lett. **98**, 043906 (2007).
27. R. Loudon, *The Quantum Theory of Light* (Oxford University, 2000).
28. J. M. Smith, G. S. Buller, D. Marshall, A. Miller, and C. C. Button, "Microsecond carrier lifetimes in InGaAsP quantum wells emitting at $\lambda = 1.5$ μm," Appl. Phys. Lett. **80**, 1870 (2002).
29. T. Erneux and P. Glorieux, "Slow passage," in *Laser Dynamics* (Cambridge University, 2010), pp. 155–171.
30. J. R. Tredicce, G. L. Lippi, P. Mandel, B. Charasse, A. Chevalier, and B. Picqué, "Critical slowing down at a bifurcation," Am. J. Phys. **72**, 799–809 (2004).
31. W. Scharpf, M. Squicciarini, D. Bromley, C. Green, J. R. Tredicce, and L. M. Narducci, "Experimental observation of a delayed bifurcation at the threshold of an argon laser," Opt. Commun. **63**, 344–348 (1987).
32. F. T. Arecchi, W. Gadomski, R. Meucci, and J. A. Roversi, "Delayed bifurcation at the threshold of a swept gain CO_2 laser," Opt. Commun. **70**, 155–160 (1989).
33. A. El Amili, G. Gredat, M. Alouini, I. Sagnes, and F. Bretenaker, "Experimental study of the delayed threshold phenomenon in a class-A VECSEL," Eur. Phys. J. **58**, 10501 (2012).
34. P. P. Baveja, B. Kögel, P. Westbergh, J. S. Gustavsson, Å. Haglund, D. N. Maywar, G. P. Agrawal, and A. Larsson, "Assessment of VCSEL thermal rollover mechanisms from measurements and empirical modeling," Opt. Express **19**, 15490–15505 (2011).
35. Q. Gu, J. S. T. Smalley, J. Shane, O. Bondarenko, and Y. Fainman, "Temperature effects in metal-clad semiconductor nanolasers," Nanophotonics **4**, 26–43 (2015).